SCIENCE CHINA
Chemistry

•ARTICLES•

January 2023 Vol.66 No.1: 202–215
https://doi.org/10.1007/s11426-022-1394-y

# Refining acceptor aggregation in nonfullerene organic solar cells to achieve high efficiency and superior thermal stability

Kaihu Xian[1], Shengnan Zhang[2,3], Ye Xu[4], Junwei Liu[1], Kangkang Zhou[1], Zhongxiang Peng[1], Mingfei Li[1], Wenchao Zhao[5], Yu Chen[6], Zhuping Fei[2,3*], Jianhui Hou[4], Yanhou Geng[1,7] & Long Ye[1*]

[1]*School of Materials Science & Engineering, Tianjin Key Laboratory of Molecular Optoelectronic Sciences, Tianjin University, and Collaborative Innovation Center of Chemical Science and Engineering, Tianjin 300350, China;*
[2]*Institute of Molecular Plus, Tianjin Key Laboratory of Molecular Optoelectronic Science, Tianjin University, Tianjin 300072, China;*
[3]*Haihe Laboratory of Sustainable Chemical Transformations, Tianjin 300192, China;*
[4]*Beijing National Laboratory for Molecular Sciences, State Key Laboratory of Polymer Physics and Chemistry, CAS Research/Education Center for Excellence in Molecular Sciences, Institute of Chemistry, Chinese Academy of Sciences, Beijing 100190, China;*
[5]*College of Materials Science and Engineering, Nanjing Forestry University, Nanjing 210037, China;*
[6]*Institute of High Energy Physics, Chinese Academy of Sciences, Beijing 100049, China;*
[7]*Joint School of National University of Singapore and Tianjin University, International Campus of Tianjin University, Binhai New City, Fuzhou 350207, China*

Received July 21, 2022; accepted September 8, 2022; published online November 23, 2022

With the rapid increase in photoelectric conversion efficiency of organic photovoltaics (OPVs), prolonging the operational lifetime of devices becomes one of the critical prerequisites for commercial applications. Guided by the theoretical calculations of molecular stacking and miscibility, we proposed an effective approach to simultaneously improve device performance and thermal stability of high-efficiency OPVs by refining the aggregation of Y-series acceptors. The key to this approach is deliberately designing an asymmetric Y-series acceptor, named Y6-CNO, which acts as a third component regulator to finely tune the degree of acceptor aggregation and crystallization in the benchmark PM6:Y6-BO system. Strikingly, a champion photovoltaic efficiency of 18.0% was achieved by introducing 15 wt% Y6-CNO into the PM6:Y6-BO system, significantly higher than the control binary cell (16.7%). Moreover, annealing at 100 °C for over 1,200 h does not markedly affect the photovoltaic performance of the optimal ternary devices, maintaining above 95% of the initial performance and exhibiting an exceptionally high $T_{80}$ lifetime of 9,000 h under continuous thermal annealing. By contrast, binary devices suffer from excessive crystallization of acceptors with long-term annealing. Additionally, mixing thermodynamics combined with morphological characterizations were employed to elucidate the microstructure-thermal stability relationships. The ternary OPVs consisting of symmetric and asymmetric homologous acceptors form better charge transport channels and can effectively suppress excessive aggregation of acceptors under long-term annealing. This work demonstrates the effectiveness of refining acceptor aggregation *via* molecular design for highly efficient and stable nonfullerene-based OPVs.

**organic photovoltaics, asymmetric acceptor, miscibility, aggregation, thermal stability**

**Citation:** Xian K, Zhang S, Xu Y, Liu J, Zhou K, Peng Z, Li M, Zhao W, Chen Y, Fei Z, Hou J, Geng Y, Ye L. Refining acceptor aggregation in nonfullerene organic solar cells to achieve high efficiency and superior thermal stability. *Sci China Chem*, 2023, 66: 202–215, https://doi.org/10.1007/s11426-022-1394-y

*Corresponding authors (email: zfei@tju.edu.cn; yelong@tju.edu.cn)

## 1 Introduction

Nowadays with the burgeoning of nonfullerene acceptor (NFA) materials [1–6], organic photovoltaic (OPV) cells exhibit great commercial application potential due to their various unique features, such as high flexibility, light weight, colorful appearance, and excellent feasibility to be translucent and wearable [7–10]. With unremitting efforts, researchers have made great progress in the design and synthesis of novel high-performance photovoltaic materials and interfacial buffer materials, the morphology modulation of active layer, the development of new device structures, and the exploration of device working mechanism [11–20]. Facilitated by these advances, the current power conversion efficiencies (PCEs) of single-junction OPVs have surpassed 19% [21–24], which can meet the commercialization threshold of solar cells. As a competitive new energy technology, it not only requires a high PCE but also needs to exhibit a long operational lifetime. Quite often, the optimal active layers based on bulk-heterojunction of organic/polymer photovoltaic materials are processed to a kinetically quenched or thermodynamically metastable state, so their microstructure will evolve over time [25–28]. Therefore, improving operation stability is one of the important frontiers for OPV research [29–33]. In practical applications, OPV cells must operate under continuous light irradiation, which will definitely cause a rapid rise in the operating temperature, and the temperature even reach ~100 °C [34]. The excessively high temperature will induce the aggregation, crystallization, or phase separation of photovoltaic materials, which accelerates the evolution of active-layer morphology and thus leads to the degradation of device performance [35–37].

The morphological evolution of active layer film under thermal stress is the central factor that determines the thermal stability of OPV cells. Typically, thermally annealing can promote molecular migration and reorganization in blend films, thereby improving the molecular order and promoting phase separation. However, such thermal annealing treatments are often performed on a short time scale (typically within 10 min or even shorter). Compared with polymer donors, small molecule acceptors in the active layers are easier to diffuse under thermal stress. The current understanding of microstructure related to the thermal stability of active layer is mainly based on a great deal of work on fullerene solar cells. Müller's group [38] has demonstrated that polymer:fullerene photovoltaic blends undergone rapid coarsening as well as the growth of micrometer-sized fullerene crystals when annealed above the glass transition temperature ($T_g$) of the components (heating the blends above 60 °C). As a result, severe phase separation and large-size fullerene crystals resulted in a sharp decline in the photovoltaic performance. While the active layers of the emerging high-efficiency systems comprising polymer donor and NFA generally have more complex microstructure [39]. NFA experiences stronger attractive forces than fullerenes, caused by π-π interactions, which will endow nonfullerene acceptors with a stronger tendency to self-aggregate and crystallize. Further, Y6 and its derivatives with superior performance can form several different polymorphs, which further complicate their microstructural analysis [40–42]. Our previous work on polythiophene and Y-series small molecule acceptors has demonstrated that long-term heating at high temperatures will induce nucleation, growth and self-aggregate excessively (agglomeration) of small molecules, which will destroy the optimal nano-network structure of the blend films created by short-term annealing [43]. Up to now, most of the studies based on Y-series NFAs focus heavily on the improvement of device efficiency. The understanding of microstructure-photoelectric property relationships related to the thermal stability of active layers based on high-performance nonfullerene solar cells remains significantly less exploration and lacks in-depth guidance. Therefore, researchers need to focus more on stabilizing the microstructure of blend films under elevated temperatures by delicately controlling the crystallization of acceptors and inhibiting agglomeration, which is the key to improve device stability of present high-performance OPVs, in particular those based on Y-series acceptors.

Accompanied by the rapid development of emerging Y-series acceptors, asymmetric molecular strategies are of great interest in recent years [44]. Asymmetric acceptors exhibit stronger binding energy and a larger dipole moment, which can exacerbate intermolecular interactions. Accordingly, the conformation effect on molecular packing, miscibility, and crystallinity can be subtly optimized [45–48]. Herein, guided by the theoretical calculations of molecular stacking and miscibility, we designed a new asymmetric NFA named Y6-CNO (Figure 1a) and simultaneously improved device efficiency and thermal stability with this new molecule. A champion PCE of 18.0% was achieved by introducing 15 wt % Y6-CNO into the benchmark PM6:Y6-BO system, which outperformed the control binary device (16.7%). We further carried out a detailed study on the underlying mechanism of why device photovoltaic performance and thermal stability were boosted. Moreover, we combined synchrotron radiation-based X-ray scattering and real-space microscopy to monitor the aggregation structure change of the ternary blend system. On this basis, we found that this $A_1$-D-$A_2$ (D: electron donor unit; A: electron acceptor unit) asymmetric structure is miscible completely with its homologous symmetric acceptor Y6-BO (also named BTP-4F-C12 [49], an analogue of Y6). However, the large-scale crystallization process will be suppressed for the conformation effect on molecular packing, miscibility, and crystallinity. As a result, the ternary devices containing asymmetric NFA maintain

above 95% of the initial performance after heating at elevated temperature (100 °C) for over 1,200 h, whereas the efficiency of the binary blend films dropped to below 87% (Y6-BO blends) and 76% (Y6-CNO blends). More strikingly, the extrapolated $T_{80}$ lifetime (*i.e.*, the time required to reach 80% of the initial PCE) of the optimal ternary PM6:Y6-BO:Y6-CNO blends is up to ~9,000 h. This facile strategy has great advantages over the previously reported ones in terms of the prolonged operational lifetime of OPVs. Note that very few studies have reported the thermal stability in OPVs with asymmetric acceptors at present, this work thus fills the knowledge gap. Given the structural diversity of asymmetric nonfullerene acceptors, this work will guide the regulation of the aggregated structure of multicomponent blend films, thereby providing a feasible strategy to simultaneously improve photovoltaic efficiency and thermal stability of OPV devices.

## 2 Results and discussion

### 2.1 Theoretical assessments of molecular stacking and miscibility

To understand the molecular interaction of various end groups on the molecular packing and miscibility of Y-series acceptors, the density functional theory (DFT) method on the B3LYP/6-31G(d,p) calculation level was performed to investigate the effect of malononitrile and carbonyl on the molecular conformation differences, as induced by the asymmetric character of Y6-CNO. To simplify the calculations, the long alkyl side chain was replaced with methyl as shown in Figure 1b (TT-O) and Figure 1c (TT-CN). The dipole moment of the two different terminal groups increases from TT-O of 4.74 Debye to TT-CN of 6.98 Debye due to the enhanced intramolecular charge-transfer effect. To further monitor the influence of asymmetric end groups combinations on molecular packing, we imitated the optimized geometry geometries of molecular packing for the two-terminal groups TT-O and TT-CN. There are three types of molecular geometries with different possible stacking combinations of the terminal groups: TT-O:TT-O (Figure 1d), TT-O:TT-CN (Figure 1e) and TT-CN:TT-CN (Figure 1f). The intermolecular complexation energy was calculated considering basis set superposition error and corrected by empirical dispersion (D3 version of Grimme's dispersion) [50]. The complexation energies of the three types of end groups combinations of the Y6-CNO molecule are −25.34, −27.46 and −29.67 kcal mol$^{-1}$, respectively. A larger dipole moment can induce a stronger dipole-dipole interaction [51–53]. It can be found that the malononitrile segments (TT-CN:TT-CN) contribute to stronger intermolecular interaction and aggregation effects, thus resulting in a more planar conformation than the carbonyl segments (TT-O:TT-O and TT-O:TT-CN). However, too strong complexation energy will make the acceptors aggregate excessively, resulting in the formation of larger crystals, which likely brings a negative effect on the stability of the devices. Compared to Y6-dimer (only TT-CN:TT-CN stacking), carbonyl combines weaker, which is expected to suppress the strong crystallization of NFAs to form large crystals.

To further understand the effect of end groups on the molecular miscibility between donor and NFAs, the Hansen solubility parameters (HSPs, listed in Table S1, Supporting Information online) of PM6 and the two NFAs (Y6-BO and Y6-CNO) was calculated according to the group additive method. Subsequently, we employed the Flory-Huggins interaction parameter ($\chi$) [54,55] to describe the molecular interactions between PM6 and the two NFAs, which can be obtained with HSPs. The calculated $\chi$ parameters are listed in Table S2. The $\chi$ values are 2.93 and 3.31 for the PM6:Y6-BO and PM6:Y6-CNO blends, respectively. According to previous thermodynamic studies [56], the higher $\chi$ indicates a stronger phase separation in the PM6:Y6-CNO blend. Moreover, the $\chi$ value is 0.01 for the blend of Y6-BO and Y6-CNO, suggesting the two homologous acceptors are highly miscible. Based on the theoretical analysis of both complexation energy and $\chi$, we surmise that incorporating an appropriate content of Y6-CNO is conducive to optimizing the phase separation and microscopic morphology of the benchmark PM6:Y6-BO system, which can suppress the degradation of device performance over time caused by the the formation of acceptor agglomerates.

### 2.2 Materials synthesis and basic properties

Motivated by the above theoretical analysis, the desired target compound Y6-CNO was designed and synthesized using a simple two-step route from the commercially available dithienothiopheno[3,2-b]-pyrrolobenzothiadiazole (BTP) core, as shown in Figure 1g. Thus, the BTP core (compound 1) was reacted with 5,6-dichloro-1,3-indanedione by Knoevenagel condensation to afford compound 2 in a yield of 64%, followed by reaction of compound 2 with 5,6-dichloro-3-dicyanomethylene-1-indanone to afford asymmetric target compound Y6-CNO in a yield of 70%. The chemical structures of obtained compounds were characterized by $^{1}$H NMR, $^{13}$C NMR and mass spectrum. The synthetic and characterization details can be found in the Supporting Information online. The successful synthesis of Y6-CNO allows us to verify the hypothesis as detailed above.

The electrochemical property of Y6-CNO was studied by cyclic voltammetry, as shown in Figure S1, Supporting Information online. The highest occupied molecular orbital (HOMO) and lowest unoccupied molecular orbital (LUMO) levels were determined to be −5.65 and −3.89 eV, respec-

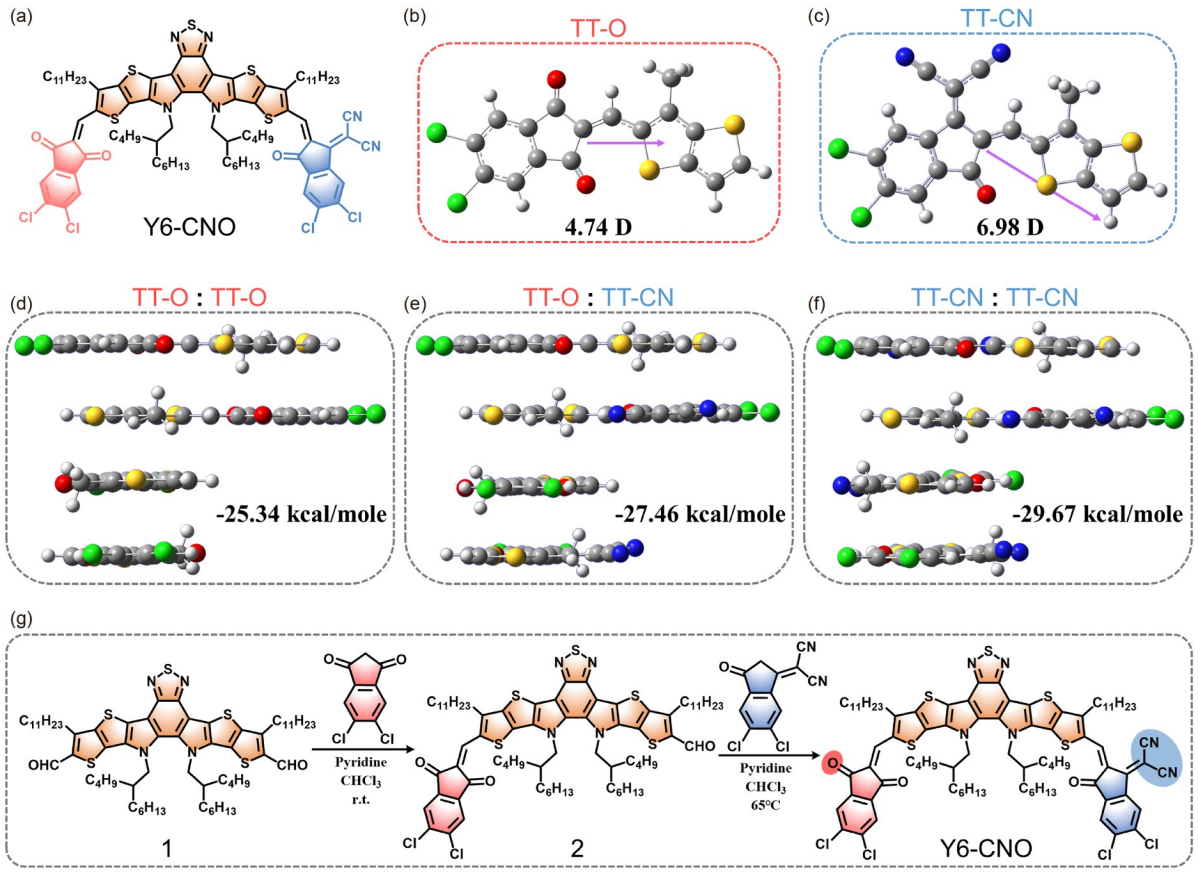


**Figure 1** (a) The chemical structure of the asymmetric nonfullerene acceptor Y6-CNO. Optimized geometries with dipole moments for the terminal parts (b) TT-O and (c) TT-CN in the asymmetric molecule. Optimized geometries of possible combinations for asymmetric acceptor dimers and corresponding intermolecular complexation energies for the regional parts of (d) TT-O:TT-O, (e) TT-O:TT-CN and (f) TT-CN:TT-CN. (g) The synthetic route to the asymmetric acceptor Y6-CNO (color online).

tively. Because of the strong electron-withdrawing of malononitrile, the substitution of carbonyl lifts the LUMO level. We selected the well-known PM6 and Y6-BO as the model system of this study, as the PM6:Y6-BO blend is one of the best performing OPV systems. The energy level alignments of all materials used in this work are illustrated in Figure 2a. Due to the substitution of carbonyl, Y6-CNO exhibits a higher LUMO level in comparison to Y6-BO (−4.06 eV), which will probably provide a larger open-circuit voltage ($V_{OC}$) relative to the Y6-BO-based binary devices.

Figure 2b presents the ultraviolet-visible (UV-vis) absorption spectra of neat PM6, Y6-BO, and Y6-CNO films. The introduction of carbonyl makes the absorption spectrum of Y6-CNO blue-shift by 43 nm in comparison with Y6-BO. Neat Y6-CNO film exhibited the characteristic absorption peak at 789 nm originating from the π-π* transition and an absorption acromion at ~700 nm, which show an analogous absorption profile to Y6-BO. The spectra of the two acceptors are complementary with that of PM6, which shows weak absorption in the lower wavelength range. The introduction of Y6-CNO further strengthens the photon harvest ability of Y6-BO in the range of 500–800 nm, which likely leads to a higher current density. Subsequently, we measured the absorption spectra of the ternary blend films with different Y6-CNO contents, as shown in Figure 2c. According to the signals of neat films, the absorption peaks at ~625 nm in the blends correspond to PM6 and the signals in the range of 700–900 nm originate from the two acceptors. It is apparent that the photon harvest and aggregation behavior of ternary blends can be finely controlled by regulating the Y6-CNO proportion of the ternary system. The aggregation features of the acceptors in the blends gradually decreases with the introduction of Y6-CNO. The relative intensity of the absorption peaks derived from the donor and acceptors were almost equal when 15 wt% of Y6-CNO is introduced (Figure S2). Meanwhile, the absorption edge gradually blue-shifted with Y6-CNO content increasing, indicating that the introduction of excess Y6-CNO will narrow the light absorption range of the blend films.

### 2.3 Photovoltaic device performance

In order to confirm the above hypothesis, a series of OPV devices were fabricated based on the PM6:Y6-BO:Y6-CNO

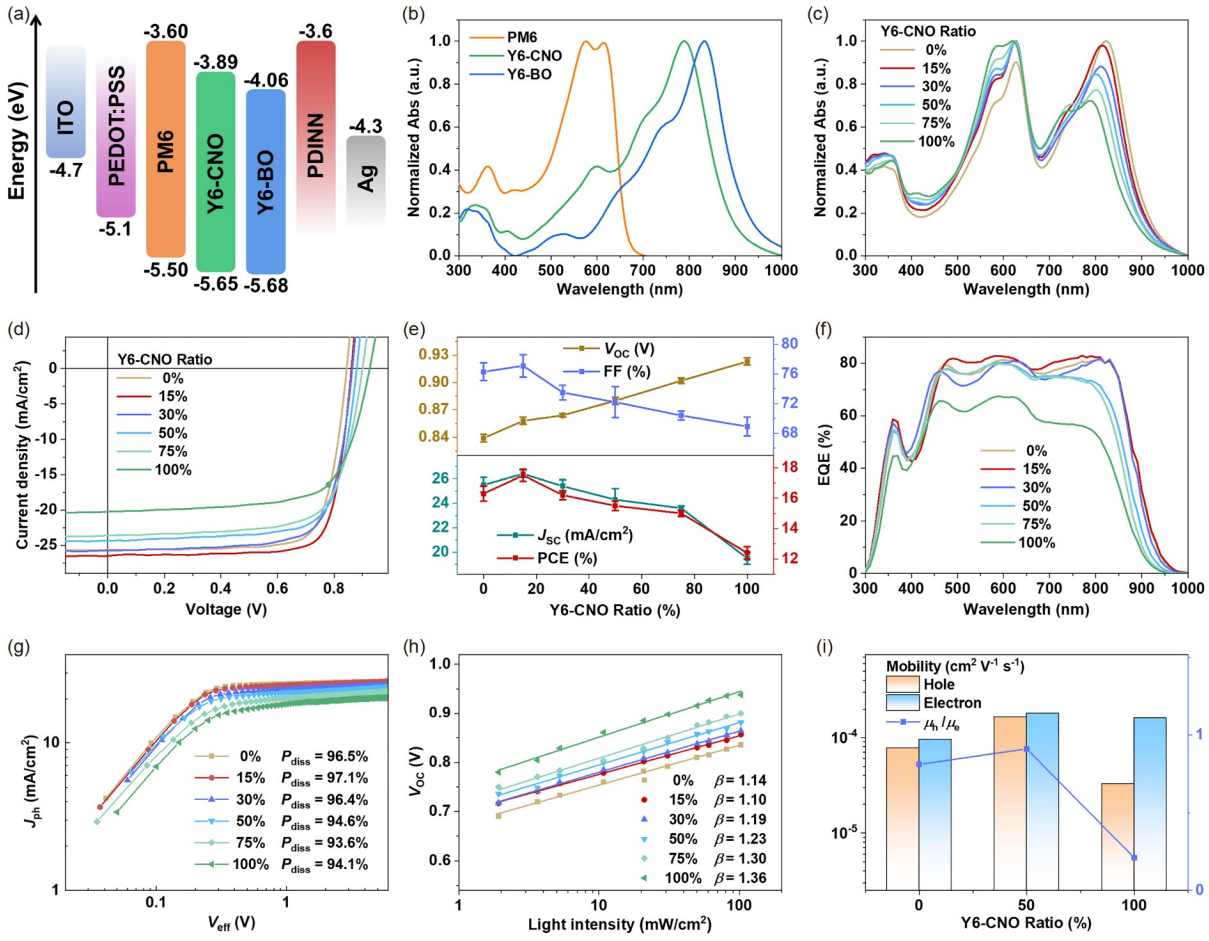


**Figure 2** (a) Schematic energy level alignment of the studied materials. (b) Normalized absorption spectra of neat PM6, Y6-BO and Y6-CNO films with thermal annealing for 10 min. (c) Absorption spectra of the PM6:Y6-BO:Y6-CNO blend films with different Y6-CNO content. (d) *J-V* characteristics under AM 1.5 G illumination with different amounts of the third component. (e) The evolution plots of $V_{OC}$, FF, $J_{SC}$ and PCE with the change of the Y6-CNO ratio. (f) The corresponding EQE curves of relevant OPVs. (g) $J_{ph}$ *versus* $V_{eff}$ plots of all devices as a function of Y6-CNO content. (h) The extracted plots of $V_{OC}$ *versus* light intensity for the devices. (i) The hole and electron mobilities of PM6:Y6-BO, PM6:Y6-CNO binary and the optimal ternary blend films (color online).

blend films with a conventional structure of indium tin oxide (ITO) glass/ poly(3,4-ethylenedioxythiophene):poly(styrene-sulfonate) (PEDOT:PSS)/ active layer/ PDINN/ Ag, where various proportions of Y6-CNO were introduced as the morphological regulator in the PM6:Y6-BO system. The weight ratio of donor to acceptors is kept constant as 1:1.2 (wt/wt) in all active layers, and the only difference is the Y6-CNO content in acceptors. The current density-voltage (*J-V*) curves of the blends under AM 1.5 G condition are shown in Figure 2d and the detailed photovoltaic parameters are summarized in Table 1. The control PM6:Y6-BO-based binary cell exhibits the minimum $V_{OC}$ of 0.845 V with a short-circuit current density ($J_{SC}$) of 25.6 mA/cm$^2$, a fill factor (FF) of 77.0% and a PCE of 16.7% which is in line with the reported value in the literature [57]. The PM6:Y6-CNO binary cell exhibits a significantly lower PCE of 13.0% with the lowest $J_{SC}$ of 20.2 mA/cm$^2$, the lowest FF of 69.4%, and the highest $V_{OC}$ of 0.926 V, which is mainly caused by the higher LUMO energy of Y6-CNO. Intriguingly, we achieved the best PCE of 18.0% with a $V_{OC}$ of 0.862 V, an FF of 78.6% and the maximum $J_{SC}$ of 26.5 mA/cm$^2$ by incorporating 15 wt% Y6-CNO in acceptors.

As can be seen from Figure 2e, the $V_{OC}$ values of ternary OPVs increased monotonically as the Y6-CNO content raised. Meanwhile, the $J_{SC}$, FF and PCE values showed slight increasing trend at first and then decreased rapidly. The external quantum efficiency (EQE) curves of the corresponding devices are presented in Figure 2f. The ternary blends with 15 wt% Y6-CNO exhibit desirable EQE values over 80% in the wavelength region of 480–830 nm. With the further introduction of Y6-CNO, the light response becomes narrower and weaker, which is matched with the absorption spectra. The calculated integrated current densities from the EQE spectra are consistent with the device $J_{SC}$ values within a 5% error range, supporting the reliability of $J_{SC}$ obtained from the *J-V* measurements.

**Table 1** Detailed photovoltaic parameters of PM6:Y6-BO:Y6-CNO-based devices with different Y6-CNO contents under AM 1.5 G illumination

| Y6-CNO (wt%) | $V_{OC}$ (V) | $J_{SC}$ (mA/cm$^2$) | $J_{cal}$ [a] (mA/cm$^2$) | FF (%) | PCE [b] (%) |
|---|---|---|---|---|---|
| 0 | 0.845 (0.839±0.004) | 25.6 (25.5±0.6) | 25.2 | 77.0 (76.3±1.2) | 16.7 (16.3±0.5) |
| 15 | 0.862 (0.858±0.004) | 26.5 (26.4±0.3) | 25.6 | 78.6 (77.1±1.5) | 18.0 (17.5±0.4) |
| 30 | 0.865 (0.864±0.002) | 25.7 (25.4±0.5) | 24.7 | 73.9 (73.5±1.0) | 16.4 (16.2±0.3) |
| 50 | 0.881 (0.880±0.004) | 24.3 (24.3±0.9) | 23.4 | 73.3 (72.2±2.1) | 15.7 (15.5±0.3) |
| 75 | 0.901 (0.902±0.003) | 23.6 (23.6±0.2) | 22.9 | 71.4 (70.4±0.6) | 15.2 (15.0±0.2) |
| 100 | 0.926 (0.923±0.004) | 20.2 (19.5±0.5) | 19.3 | 69.4 (68.9±1.3) | 13.0 (12.4±0.4) |

a) $J_{cal}$ is calculated by the EQE curve; b) The average values of the photovoltaic parameters are obtained from 6 devices.

### 2.4 Charge separation and collection behaviors

To clarify the reasons for the performance improvement, we further investigated the charge separation and collection properties of devices. The analysis of photocurrent density ($J_{ph}$) *versus* effective voltage ($V_{eff}$) was performed to study the exciton dissociation processes. $J_{ph}$ is the difference between the current density in the dark and under illumination; $V_{eff}$ is the difference between the voltage when $J_{ph}$ is zero and the applied voltage. The exciton dissociation probability ($P_{diss}$) is defined as the ratio of $J_{ph}/J_{sat}$ ($J_{sat}$ represents the saturation current density). As shown in Figure 2g, the $J_{ph}$ of all the devices saturates well at a low $V_{eff}$ with all $P_{diss}$ values above 90%, which indicates that the charge separation in all devices is efficient. The introduction of 15 wt%-Y6-CNO promotes the exciton dissociation according to the slightly increased $P_{diss}$ (97.1%). Such effective exciton dissociation is favorable for achieving higher currents.

We then analyzed the charge recombination behavior by measuring the $J_{SC}$ and $V_{OC}$ of devices under varying light intensity ($P_{light}$). It has demonstrated that the slope ($\alpha$) of $J_{SC}$ *versus* $P_{light}$ can provide insight into the bimolecular recombination. The relationship can be expressed as $J_{SC} \propto P_{light}^{\alpha}$, where weak bimolecular recombination would lead to a linear dependence with the exponential factor $\alpha$ value approaching 1 [58]. As shown in Figure S3, all the devices herein show a linear dependence of $J_{SC}$ on the $P_{light}$ with a slope above 0.98 and the $\alpha$ value first increases and then decreases slightly with the Y6-CNO content increasing. It indicates that bimolecular recombination is relatively weak and does not play a significant role in the devices. The geminate or Shockley-Read-Hall recombination is extracted from the dependence of $V_{OC}$ on $P_{light}$. The relationship between $V_{OC}$ and $P_{light}$ can be expressed as $V_{OC}=\beta(kT/e)\ln(P_{light})+c$, where $k$ is the Boltzmann constant, $T$ is the absolute temperature, $e$ is the elementary charge, $c$ is constant, and $\beta$ is the scaling factor. Typically, a slope of 1 $kT/e$ illustrates that bimolecular recombination is the dominating mechanism. In contrast, a slope of 2 $kT/e$ represents that trap-assisted recombination is the dominating mechanism [59,60]. As shown in Figure 2h, all the devices demonstrate a recombination mechanism of trap-assisted processes under open-circuit conditions. The $\beta$ value of 1.10 for the optimized ternary cell with 15 wt% Y6-CNO content is smaller than that of 1.14 for the PM6:Y6-BO binary device and 1.36 for the PM6:Y6-CNO binary cell, indicating that trap-assisted recombination can be restrained in the optimized ternary cell. The $\beta$ value gradually increased with higher Y6-CNO content (>30%), which indicated that the addition of a large amount of the third component not only fails to fill the defects in the films but also forms more defects. All the recombination behaviors indicate that recombination is minimized with a small amount of the third component while a large amount of the third component will promote recombination rapidly.

Subsequently, we investigated the charge carrier transport properties of the two binary and the best ternary devices. The hole and electron mobilities were measured by the space charge limited current (SCLC) method, and the corresponding mobility data are exhibited in Figure S4 and Table S3. The plots of hole and electron mobilities with different Y6-CNO content are expressed in Figure 2i, from which the optimal ternary film can be found with the highest mobility and the lowest $\mu_h/\mu_e$ (the ratio of hole and electron mobilities; the closer the value is to 1, the more balanced the charge transport is), indicative of most intensive and balanced charge transport.

### 2.5 Phase separation and crystallization behavior

The formation of defects is closely related to film morphology. To gain a deep understanding of the phase separation of blend films, atomic force microscopy (AFM) was used to capture the surface morphologies of PM6:Y6-BO,

PM6:Y6-CNO binary and optimal PM6:Y6-BO:Y6-CNO ternary (15 wt% of Y6-CNO was introduced as the third component, hereafter denoted as 15%-Ternary) blend films. Considering that 15 wt% Y6-CNO led to the largest improvement in the photovoltaic performance of ternary devices, we selected the ternary blends with 15 wt%-third content to investigate the performance differences between ternary and binary blend films. As presented in Figure 3a, the PM6:Y6-BO-based binary blend film exhibited uniform and smooth fibrillar surfaces with a root-mean-square surface roughness ($R_q$) of 1.0 nm, which is almost identical to those of high-efficiency PM6:Y-series systems reported in the literature [61,62]. The uniform and smooth surface implied that a good network interpenetrating with proper phase separation was well-formed in the film. In contrast, PM6:Y6-CNO-based film (Figure 3b) showed an excessive phase separation morphology with a large $R_q$ of 3.9 nm, which agrees well with the higher $\chi$ parameter. The appearance of the large agglomerates clarifies the origin of the poor performance of PM6:Y6-CNO-based binary devices. As a comparison, the $R_q$ of 15%-Ternary blend film was slightly increased to 1.1 nm with a similar surface morphology with PM6:Y6-BO blend film as shown in Figure 3c. Similarly, the bulk morphology of the three blends under optimal conditions (annealing for 10 min) monitored by transmission electron microscopy (TEM) also showed the same morphological characteristics as the surfaces (Figure S5).

To quantitatively attain the domain size of phase separation within the blend films, we obtained the power spectral density (PSD) profiles by fast Fourier transform analysis of the AFM phase images. As a powerful method to quantitatively describe the distribution of surface morphology and texture of organic electronic films, the PSD analysis converts the fluctuations of the surface morphology into the intensity spectrum distribution in the specified spatial frequency space [63–65]. As displayed in Figure 3d, the three blend films

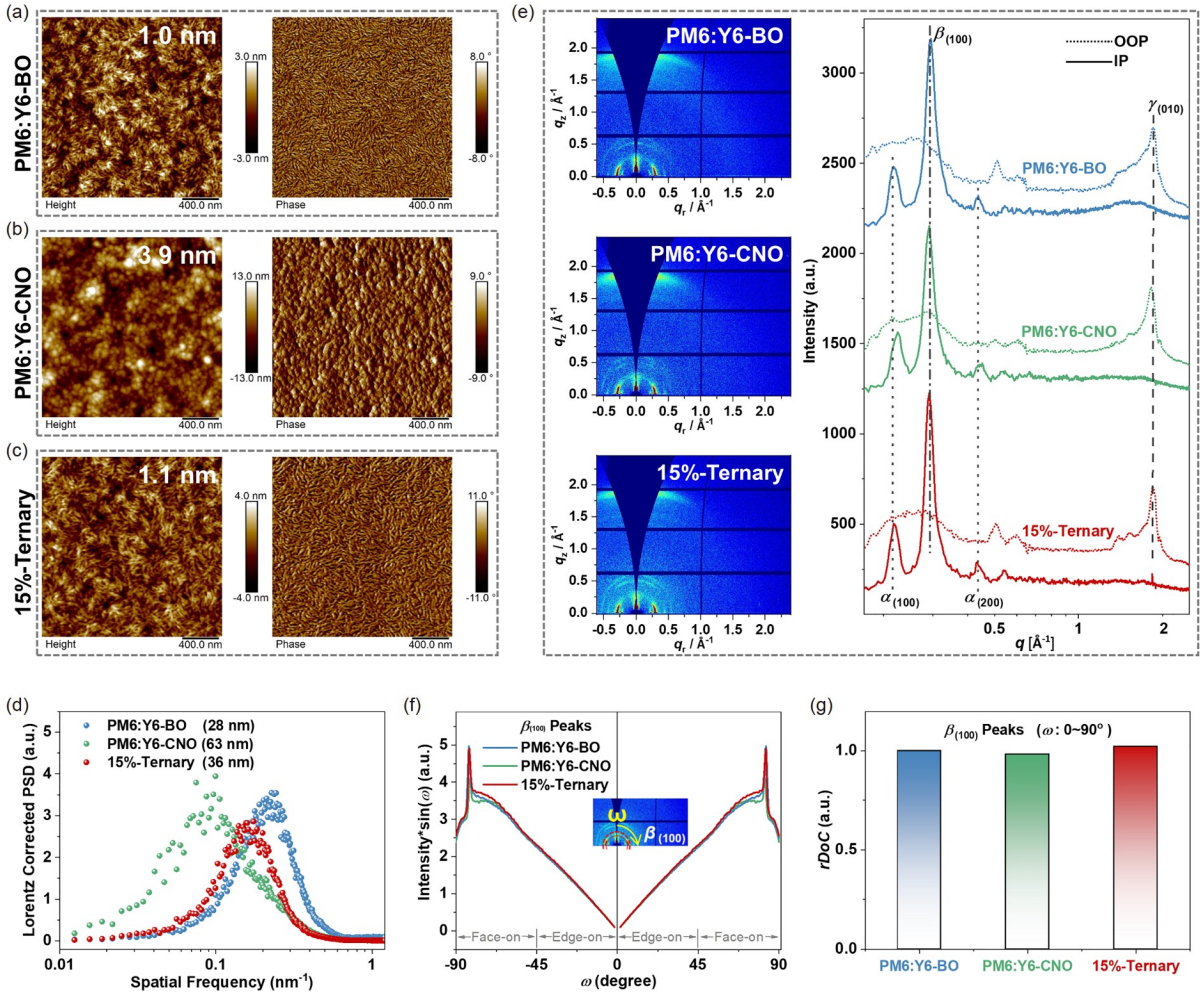


**Figure 3** The AFM height and phase images of (a) PM6:Y6-BO, (b) PM6:Y6-CNO binary and (c) 15%-Ternary blend films, The $R_q$ data are listed. (d) Lorentz corrected PSD profiles of the AFM phase images for the blend films. (e) The 2D GIWAXS patterns of PM6:Y6-BO, PM6:Y6-CNO and 15%-Ternary blend films, and the corresponding out-of-plane (dotted lines) and in-plane (solid lines) sector-averaged profiles for the three blend films. All the films were annealed for 10 min. (f) Pole figures of $\beta$(100) stacking peaks of the three blends. (g) The histogram of rDoC values of $\beta$(100) peaks of the three blends (color online).

show one characteristic peak and the corresponding average feature domain monotonically coarsened. Obviously, there is no extra domain formed with the introduction of Y6-CNO. The domain sizes of blend films were 28, 36 and 63 nm when 0%, 15%, 100% Y6-CNO content are used. The introduction of a small amount of Y6-CNO slightly improves the phase separation of the films while maintaining the original efficient transport channels of the PM6:Y6-BO binary system, resulting in more efficient charge separation and extraction. Therefore, Y6-CNO can act as a third component regulator to finely modulate the acceptor aggregation in high-efficiency binary systems.

Having analyzed the mesoscale bulk morphology, we proceed to probe the effect of the Y6-CNO content on crystallinity and molecular stacking in the blend films by grazing incidence wide-angle X-ray scattering (GIWAXS) measurements [66–69]. The 2D GIWAXS patterns and the corresponding out-of-plane (OOP) and in-plane (IP) profiles of optimal PM6:Y6-BO, PM6:Y6-CNO and 15%-Ternary blend films are shown in Figure 3e, and the detailed parameters are summarized in Tables S4, S5. The three blend films show very little difference in diffraction signals, and the as-cast neat film of Y6-CNO exhibits a similar crystalline form to the neat Y6-BO film (Figure S6), which together suggests that the substitution of carbonyl does not change the molecular orientation significantly. All the blend films exhibit multiple strong (100) diffraction peaks in IP directions and an overlapped (010) diffraction peak in OOP directions, indicating a predominant face-on molecular orientation. Such a face-on orientation is more conducive to the charge transport within the OPV films [70–72]. Obviously, there are several different polymorphs formed in the three blends. For example, the diffraction peak at 0.22 $Å^{-1}$ in IP directions corresponds to the $\alpha_{(100)}$ reflection from the alkyl-stacking direction originated from the acceptors and the peak at ~0.29 $Å^{-1}$ can be assigned to the $\beta_{(100)}$ reflection. A weak peak appeared at $q_z$=0.44 $Å^{-1}$ can be assigned to the $\alpha_{(200)}$ reflections. The peak at $q_z$=~1.85 $Å^{-1}$ in OOP directions can be assigned to the $\gamma_{(010)}$ π-π stacking reflection of acceptors. It should be highlighted that all the peaks in OOP directions can be slightly shifted toward smaller diffraction vector ($q$) values along with the incorporation of more Y6-CNO. From PM6:Y6-BO to 15%-Ternary, to PM6:Y6-CNO, the blends showed increased lamellar stacking (the peak appears at ~0.50 $Å^{-1}$) distance from 12.31 to 12.45, to 12.69 Å, indicating the molecular packing in the alkyl-stacking direction becomes looser with the increase of the Y6-CNO content in the blend films. Meanwhile, the coherence length ($CL$) of lamellar stacking peaks decreased from 130.7 to 124.8, to 49.9 Å. Likewise, the π-π stacking (the peak at ~1.85 $Å^{-1}$) distance increased slightly from 3.38 to 3.39, to 3.44 Å and the CL values of π-π stacking decreased slightly from 50.5 to 46.6, to 40.5 Å, indicating the molecular π-π packing becomes looser with the Y6-CNO content increasing. Additionally, the stacking distance in the IP directions did not change significantly.

To quantify and further corroborate the effects of Y6-CNO on crystallinity and orientation of the three blends, we further performed pole figures analysis of the $\beta_{(100)}$ lamellar stacking scattering peaks in IP directions in the optimized conditions. As depicted in Figure 3f, the intensity of the pole figure of 15%-Ternary blend film was increased in face-on crystallite orientations than PM6:Y6-BO (Figure S7), while the intensity of the pole figure of PM6:Y6-CNO blend was decreased. Correspondingly, the intensity of the pole figure of PM6:Y6-CNO blend was increased in edge-on crystallite orientations than PM6:Y6-BO. The relative degree of crystallinity ($rDoC$) [73–75], which can be used to described the degree of crystallinity, is calculated by integrating the scattering intensity of the pole figure (intensity×sin($\omega$)~$\omega$) across all polar angles ($\omega$) from 0° to 90° based on a corrected Ewald sphere. The histogram of $rDoC$ values of $\beta_{(100)}$ peaks of the three blend films are depicted in Figure 3g. All values are normalized to PM6:Y6-BO blends. Upon annealing for 10 min, the $rDoC$ value of 15%-Ternary blend was slightly increased, suggesting an increase in crystallinity. While the $rDoC$ value of PM6:Y6-CNO blend was slightly decreased, indicative of a decrease in crystallinity.

Notably, the introduction of Y6-CNO mainly affects the tightness of the molecular arrangement. The introduction of a small amount of Y6-CNO slightly improves crystallinity and face-on crystallite orientations. While excessive Y6-CNO will reduce the crystallinity and lead to an increase in edge-on crystallite orientations. The excessively loose packing of PM6:Y6-CNO likely brought about the excessive phase separation of blend film, which resulted in severe trap-assisted recombination and hindered device efficiency. By comparison, the phase separation of the 15%-Ternary blend was moderately improved over the PM6:Y6-BO blend due to the slightly increased crystallinity and face-on crystallite orientations, which exhibited optimal photovoltaic efficiency. Based on AFM and GIWAXS results, the phase separation and crystalline order of the ternary system could be finely controlled by regulating the proportion of third component homologous asymmetric acceptor.

### 2.6 Thermal stability and its origins

After explaining the performance difference, we direct our attention to a more crucial aspect of OPVs, *i.e.*, thermal stability. Thermal stability of the three kinds of devices was studied in details. Since the migration and crystallization of the molecules in the active layer films is mainly driven by heat, the films were annealed at 100 °C for a long time to accelerate the aggregation and crystallization before the deposition of interface layer and metal electrode. Then, we

monitor the PCE of the overall devices over extended periods of time, as shown in Figure 4a. Such investigation excludes the chemical/physical effects of interface layer and metal electrode, which allows us to evaluate the thermal stability of the blend morphology itself independently. The experiments can exclusively reveal the effect of material crystallization due to thermal stress on the morphology and microstructure of the active layer. All device efficiencies improved a bit after annealing for 10 min (Figure S8), indicating that short-term annealing can properly promote the crystallization of molecules and form better transport channels. All efficiencies are normalized to the maximum efficiencies at 10 min. Unfortunately, the PCE dropped to 87% of the initial value when annealing over 1,200 h for PM6:Y6-BO blend films, which will be explained further below. Furthermore, the PCE of PM6:Y6-CNO-based blend films dramatically degraded to below 76% of the initial value when the annealing time was over 1,200 h. It suggests that prolonged annealing exacerbates various chaotic packing forms in the films, forming more defects, and leading to more severe recombination. In stark contrast, the 15%-Ternary blends exhibited greatly improved thermal stability, remaining 95% of the initial efficiency upon continuous heating at 100 °C for 1,200 h. Meanwhile, we further analyzed the extrapolated $T_{80}$ lifetime [76]. The results for PM6:Y6-BO:Y6-CNO based devices exhibited an impressive extrapolated $T_{80}$ lifetime of up to ~9,000 h for the optimal ternary, compared with the much shorter $T_{80}$ lifetime of ~4,200 h for PM6:Y6-BO and ~200 h for PM6:Y6-CNO binary. It indicates that the introduction of a small amount of Y6-CNO can retain the original high-efficiency morphology while stabilizing the morphology. Thus, the film offers higher thermal stability.

To understand the origin of different thermal stability of the binary and ternary OPVs, differential scanning calorimetry (DSC) measurements were performed to investigate the molecular interactions and miscibility between the donor and the acceptors [77,78]. As shown in Figure 4b, the neat Y6-BO shows a weak exothermic signal, and the corresponding crystallizing temperature is ~60 °C. The neat Y6-CNO shows a strong exothermic signal, corresponding to a higher crystallizing temperature of ~95 °C. Moreover, the crystallizing signal can be also observed for PM6:Y6-CNO blend. While no endothermic or exothermic signals can be observed for PM6:Y6-BO and 15%-Ternary blends, indicating Y6-CNO has lower miscibility than Y6-BO with PM6, which is consistent with the theoretically calculated $\chi$. Therefore, we reasonably speculate that the introduction of the third component inhibits the acceptor crystallization in the binary system. Suppression of strong crystallization can suppress the high crystallinity of acceptor in the film, thereby providing a more stable film morphology, which will synergistically lead to higher device performance and thermal stability.

Subsequently, we characterized the aggregation behavior of the two neat acceptors Y6-BO and Y6-CNO in the films with different annealing times by acquiring the UV-vis absorption spectra. As shown in Figure 4c, the maximum absorption peak of Y6-BO gradually red-shifts with annealing, from 816 nm for as-cast to 831 nm for 1 min, to 832 nm for 10 min, indicating that the acceptors rapidly aggregate and crystallize within the first minute and molecular aggregation is gradually enhanced with annealing, which will lead to the enhanced molecular crystallization. Annealing in a short time (within 10 min) can make the acceptor aggregate and crystallize moderately, which is conducive to building a better transport channel and achieving a higher PCE. With further longer annealing time, the maximum absorption peak gradually red-shift from 834 nm for 1 h to 837 nm for one day (24 h), which indicated that the aggregation and crystallization increased continuously with annealing. The excessive aggregation will lead the acceptors to form agglomerates [79–82], disrupting the original interpenetrating network structure, which leads to degradation of device performance. The neat Y6-CNO films exhibit the same aggregation properties as Y6-BO (Figure 4d). Moreover, the maximum absorption peak of Y6-CNO still significantly red-shift from 793 nm for 1 h to 805 nm for one day due to the chaotic packing, which leads to the serious performance degradation. In sharp contrast, as displayed in Figure 4e, although the short-term annealing caused a significant red-shift from 813 nm for as-cast to 829 nm for 10 min in the blend films of the two acceptors, the maximum absorption peak remained at 831 nm for 1 hour even after annealing for one day. It also demonstrated that the introduction of Y6-CNO inhibited the excessive aggregation of Y6-BO.

Significant differences in aggregation properties of the acceptors will result in different changes in film microstructure. To elucidate the microstructural changes of binary and ternary blend films during prolonged annealing, we investigated the bulk morphology of the three blends with thermal annealing at 100 °C for one day (24 h) *via* TEM. PM6:Y6-BO blend film still retains its nanofibrous structure as shown in Figure 5a, while island-like agglomerates appeared within the entire film after annealing for one day, which is the main reason for its device efficiency decline. As shown in Figure 5b, the excessive phase separation of PM6:Y6-CNO blend film becomes more severe, indicating that annealing exacerbates the chaotic stacking pattern; which makes a large drop in the device efficiency. Intriguingly, upon the addition of 15 wt% Y6-CNO into PM6:Y6-BO system (Figure 5c), the nanofibrous structures are still evident and no apparent acceptor agglomeration is observed. In addition, we also observed the same regularity through the surface morphologies of the three films (Figure S9) monitored by AFM with thermal annealing for one day. It indicated that the introduction of the asymmetric structured

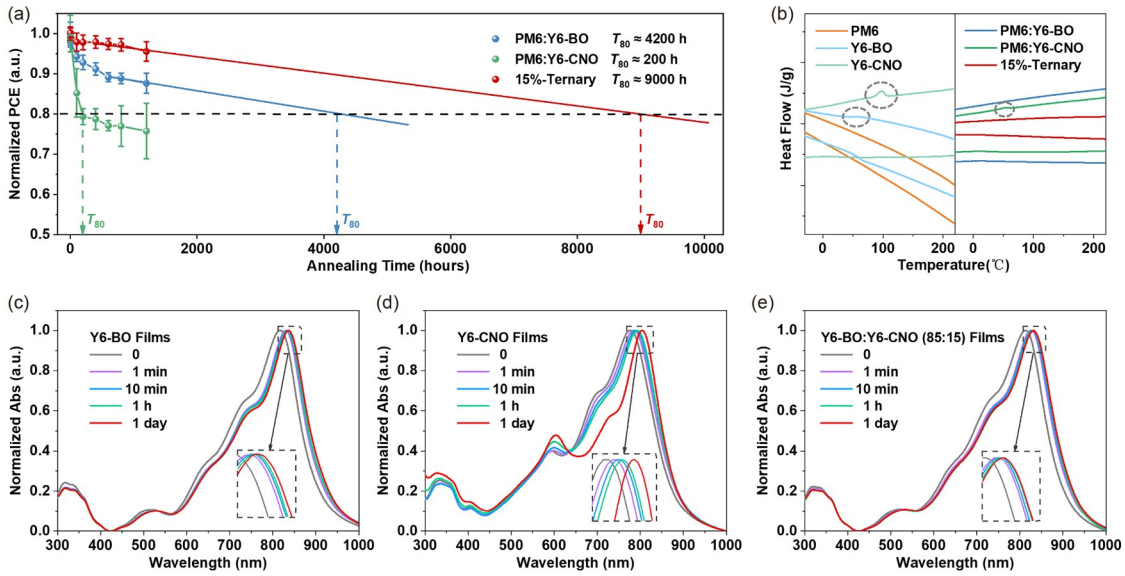


**Figure 4** (a) The evolution plots of normalized PCE for the three blend films under continuous thermal annealing at 100 °C and the extrapolated $T_{80}$ lifetime. The vertical and dashed arrows mark the $T_{80}$ of the three blends. (b) DSC curves of neat materials and their blends. Normalized absorption spectra of (c) Y6-BO, (d) Y6-CNO neat films and (e) Y6-BO:Y6-CNO (85:15) blend films with different annealing times (color online).

third component can well inhibit the excessive aggregation of acceptors in the binary systems, thus improving the morphology stability of the blend films, which affords better thermal stability of the devices.

Furthermore, we employed GIWAXS to investigate the influence of Y6-CNO on the crystalline properties of the PM6:Y6-BO-based blend films with long-term annealing. The 2D GIWAXS patterns and the corresponding OOP and IP sector-averaged profiles for the three blend films with annealing for one day are displayed in Figure 5d–h. Besides, the profiles of the three films annealed for 10 min are also presented for comparison. Unfortunately, the signal of PM6 is overlaid by the signal of the acceptors, making it difficult to analyze the aggregation behavior of PM6 alone. Nonetheless, we can reasonably speculate from the miscibility analysis that the change of the π-π stacking signals is mainly caused by the crystallization behavior of the acceptors, according to the nearly invariant crystallization signal of PM6 (Figure S10). It is obvious that the diffraction intensity of PM6:Y6-BO binary films is significantly enhanced in both OOP and IP directions. The area of π-π stacking signals, $\gamma_{(010)}$ diffraction peaks in OOP directions, increased by a factor of ~2 (Tables S6, S7), indicating the significant enhancement of acceptor crystallization. Excessive crystallization of the acceptors leads to the formation of large-sized island-like agglomerates. On the contrary, the diffraction intensity of PM6:Y6-CNO binary film slightly weakens with the prolongation of annealing time according to the area of π-π stacking signals decreased a little bit. Although the aggregation of molecules is the most significant for the sharply red-shifted spectra, this aggregation is randomly and coexisting in multiple packing forms, resulting in weakened molecular crystallization signals. The molecular packing in the film is already very chaotic, and the continuous annealing exacerbates its chaos, which is also the reason for the worst device stability. Satisfactorily, although the diffraction intensity of the 15%-Ternary blend film is also enhanced slightly according to the slightly increase in π-π stacking area, the enhancement is very limited and significantly smaller than that of the PM6:Y6-BO binary films, which indicated that the crystallization of the acceptor in the original binary system is obviously inhibited.

To quantify the changes in crystalline morphology of the three blends, we further performed pole figures analysis (Figure 5i) of the $\beta_{(100)}$ lamellar stacking peaks under the thermal stress as a function of annealing time. As depicted in Figure 5j, the intensities of the pole figures of PM6:Y6-BO and 15%-Ternary blends were increased in face-on crystallite orientations under the thermal stress. The histogram of *rDoC* values of $\beta_{(100)}$ peaks of the three blends are depicted in Figure 5k. All the *rDoC* values are normalized to PM6:Y6-BO blends with annealing for 10 min. Obviously, the *rDoC* value of PM6:Y6-BO-based blend film with annealing for one day increases significantly and is the highest, indicating that it has the strongest molecular packing. Such a high crystallinity enhancement implies excessive crystallization of the acceptor molecules, which leads to the formation of agglomerates. While the crystallinity enhancement in the 15%-Ternary blend is suppressed, which keeps the original favorable nanofiber network structure. On the contrary, the *rDoC* value of PM6:Y6-CNO blend film hardly increases and the face-on crystallite orientations slightly weakens with

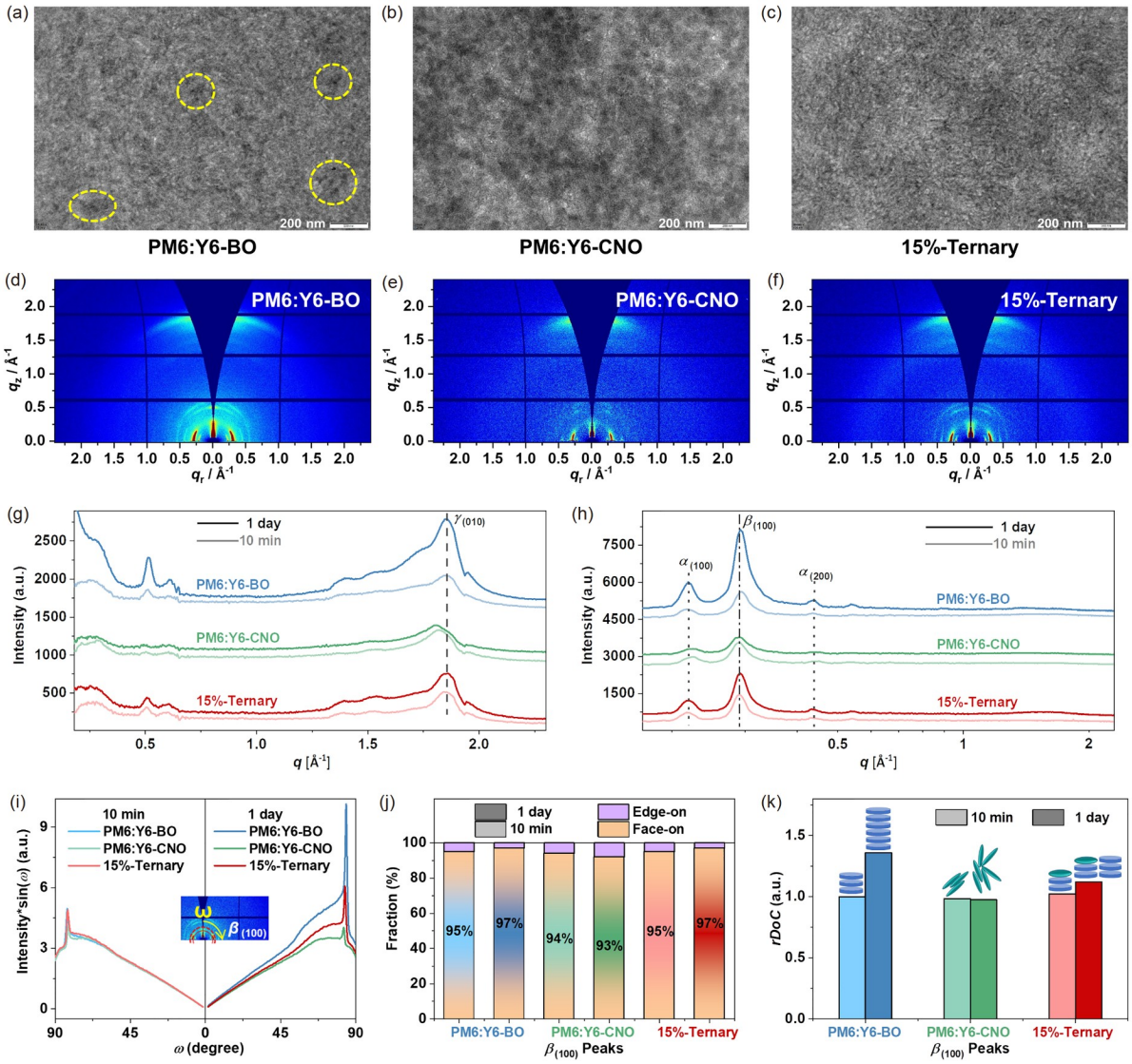


**Figure 5** The TEM images of (a) PM6:Y6-BO, (b) PM6:Y6-CNO binary and (c) 15%-Ternary blend films. All the films were annealed for one day. The 2D GIWAXS patterns of (d) PM6:Y6-BO, (e) PM6:Y6-CNO and (f) 15%-Ternary blend films with annealing for one day. The corresponding (g) out-of-plane and (h) in-plane sector-averaged profiles for the three blend films. Note that the profiles of the three films annealed for 10 min are also presented for comparison. (i) Pole figures of $\beta_{(100)}$ stacking peaks of the three blends with different annealing time. (j) The histogram of face-on/edge-on fractions of the three blends. (k) The histogram of *rDoC* values of $\beta_{(100)}$ peaks of the three blends. Note that ⬭ denotes Y6-BO and ⬭ represents Y6-CNO, and the packing models of the two acceptors within the six films are presented.

long-term annealing, indicating that the continuous annealing makes molecular arrangement in the film more chaotic.

## 2.7 Microstructure-stability relationships

Finally, we attempted to connect molecular stacking behaviors and morphological properties with device performance and thermal stability by assessing the analysis of the above experimental results collectively. Due to the similar chemical structure, the two acceptor molecules have similar stacking patterns and crystal forms. Moreover, due to the differences in end groups, the two acceptors exhibit very different aggregation characteristics. When the as-cast films were thermally annealed in a short time (10 min), both acceptor molecules will rapidly aggregate and crystallize significantly, which shift the photovoltaic performance of both binary devices to their optimum. With further longer annealing, the symmetrical Y6-BO molecules continue to aggregate and crystallize, forming overlarge agglomerates. While asymmetric Y6-CNO molecules can only clump together randomly, which is a chaotic aggregation and different from crystallization.

The schematic diagrams of the acceptors stacking with long annealing time are displayed in Figure 6. Combined with the theoretical calculation results above, we can speculate that when there is only one symmetric acceptor in the

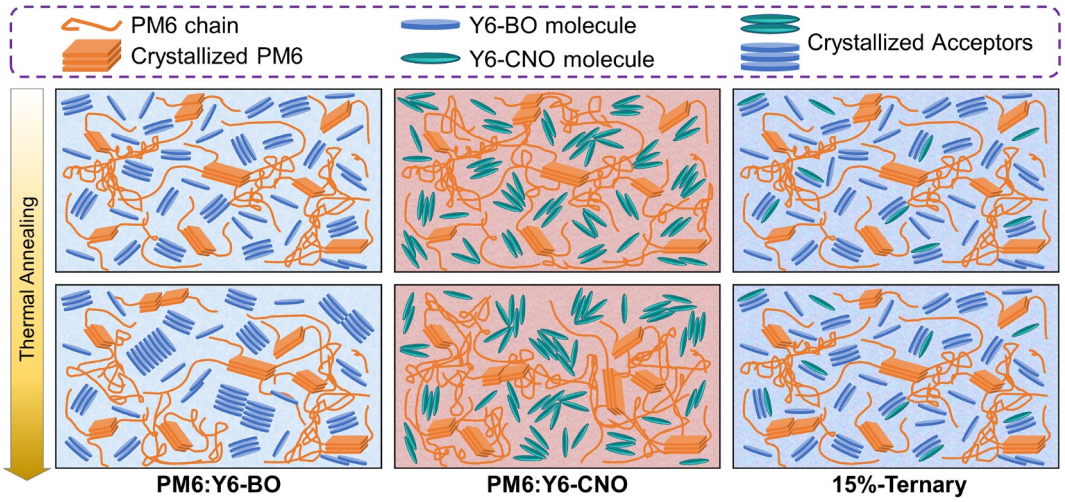


**Figure 6** Schematic illustrations of the acceptors stacking within the three blend films with optimal and long annealing times (color online).

system (*i.e.*, PM6:Y6-BO blend), the acceptors will continue to tightly pack to form more crystals and larger agglomerates with long-term annealing. Such overlarge agglomerates will destroy the original network interpenetrating structure in the films, resulting in the degradation of device performances. On the other hand, there is more than one type of stacking within the PM6:Y6-CNO film. Although the acceptor molecules have the strongest self-aggregation degree within the film, this self-aggregation of randomly stacked molecules limits the crystal growth. It prevents a good transport structure from being formed inside the device from the beginning, resulting in the lowest device performance. Also, prolonged heating exacerbates this chaotic aggregation, leading to the worst device thermal stability.

However, when small amounts of homologous asymmetric acceptor is introduced into the system, the original nanofiber morphology within the high-efficiency binary system is not affected, and the molecular orientation does not change significantly. Furthermore, the two acceptors cannot be stacked too much to form agglomerates with long-term heating, resulting from the existence of asymmetric end groups. Due to the difference in complexation energies, Y6-CNO molecule would preferentially stack with Y6-BO (TT-CN:TT-CN and TT-O:TT-CN combinations) rather than self-stacking (TT-O:TT-O and TT-O:TT-CN combinations). Furthermore, due to the lower complexing energy, the combinations of the TT-O end groups are easily broken by heat, thus preventing the acceptors molecules from continuously staking to aggregate and crystallize excessively, forming agglomerates. The inhibition of excessive stacking of acceptor molecules still maintains the original morphology of the film, which also results in better thermal stability of the films.

Whereas the intrinsic degradation mechanisms caused by the light absorption (result in high operating temperature) of active layers, which cannot be overcome within the original binary systems. Our work is evidencing light up to the evolution of active layers microstructure (caused by excessive self-aggregation and crystallization of acceptors) as the dominant origin for device performance degradation. Based on our photovoltaic and morphological analysis, stablized morphology need to be established in order to attain highly efficient and thermally stable OPVs. Asymmetric end groups allow two acceptor molecules to have similar structures and crystalline forms but only differ in aggregation characteristics, which avoids the uncertainty and uncontrollability of the morphology caused by the new crystallization when introduced a very different guest. The constant photovoltaic performance of ternary devices at 100 °C confirms that using homologous symmetric and asymmetric acceptor mixtures to refining acceptor aggregation is a powerful strategy to improve the thermal stability of OPV cells.

## 3 Conclusions

Based on the design and introduction of a novel asymmetric acceptor Y6-CNO, we proposed an effective strategy to simultaneously improve device efficiency and thermal stability by blending this asymmetric NFA with its homologous symmetric acceptor (Y6-BO). As Y6-CNO is highly miscible with Y6-BO, it can act as a third component regulator to finely tune the degree of acceptor aggregation and crystallization in the high-efficiency PM6:Y6-BO system. With this benefit, a champion PCE of 18.0% was achieved by introducing 15 wt% Y6-CNO into the PM6:Y6-BO system, which was much higher compared with PM6:Y6-BO binary

device (16.7%). The introduction of a small amount of the third component enables the formation of better transport channels in the film and can effectively suppress the excessive aggregation of acceptors with long-term annealing. As a result, the optimal ternary devices maintain above 95% of the initial performance after annealing for at least 1,200 h at 100 °C, and the extrapolated $T_{80}$ lifetime reaches over 9,000 h. Our results thus emphasize the effectiveness of refining acceptor aggregation and crystallization *via* molecular design. It also shines light on the crucial importance of understanding microstructure-photoelectric property relationships in the quest for high-performance and highly stable OPVs. Moreover, molecular stacking simulations and miscibility calculation will be useful to assess the operational lifetime of systems and to design superior new materials. Further thoughts have to be given to the evolution mechanism of active layers microstructure under various stresses. That is of particular interest for the design of long-term stable devices toward scale-up.

**Acknowledgements** This work was supported by the National Natural Science Foundation of China (52073207, 52121002) and the Fundamental Research Funds for the Central Universities. L. Ye also appreciates the Peiyang Scholar Program of Tianjin University for support. Z. Fei and S. Zhang thank the Haihe Laboratory of Sustainable Chemical Transformations for financial support. GIWAXS data acquisition at the beamline BL16B1 of Shanghai Synchrotron Radiation Facility (SSRF). Besides, the GIWAXS data were also checked at the beamline BL14B1 of SSRF and the beamline 1W1A of Beijing Synchrotron Radiation Facility (BSRF).

**Conflict of interest** The authors declare no conflict of interest.

**Supporting information** The supporting information is available online at http://chem.scichina.com and link.springer.com/journal/11426. The supporting materials are published as submitted, without typesetting or editing. The responsibility for scientific accuracy and content remains entirely with the authors.

1 Li S, Li CZ, Shi M, Chen H. *ACS Energy Lett*, 2020, 5: 1554–1567
2 Cheng P, Li G, Zhan X, Yang Y. *Nat Photon*, 2018, 12: 131–142
3 Wan X, Li C, Zhang M, Chen Y. *Chem Soc Rev*, 2020, 49: 2828–2842
4 Wadsworth A, Moser M, Marks A, Little MS, Gasparini N, Brabec CJ, Baran D, McCulloch I. *Chem Soc Rev*, 2019, 48: 1596–1625
5 Zhang ZG, Li Y. *Angew Chem Int Ed*, 2021, 60: 4422–4433
6 Liu Y, Liu B, Ma CQ, Huang F, Feng G, Chen H, Hou J, Yan L, Wei Q, Luo Q, Bao Q, Ma W, Liu W, Li W, Wan X, Hu X, Han Y, Li Y, Zhou Y, Zou Y, Chen Y, Li Y, Chen Y, Tang Z, Hu Z, Zhang ZG, Bo Z. *Sci China Chem*, 2021, 65: 224–268
7 Li Y, Xu G, Cui C, Li Y. *Adv Energy Mater*, 2018, 8: 1701791
8 Meng X, Zhang L, Xie Y, Hu X, Xing Z, Huang Z, Liu C, Tan L, Zhou W, Sun Y, Ma W, Chen Y. *Adv Mater*, 2019, 31: 1903649
9 Zhang K, Chen Z, Armin A, Dong S, Xia R, Yip HL, Shoaee S, Huang F, Cao Y. *Sol RRL*, 2018, 2: 1700169
10 Liu Y, Liu B, Ma CQ, Huang F, Feng G, Chen H, Hou J, Yan L, Wei Q, Luo Q, Bao Q, Ma W, Liu W, Li W, Wan X, Hu X, Han Y, Li Y, Zhou Y, Zou Y, Chen Y, Liu Y, Meng L, Li Y, Chen Y, Tang Z, Hu Z, Zhang ZG, Bo Z. *Sci China Chem*, 2022, 65: 1457–1497
11 Zuo L, Jo SB, Li Y, Meng Y, Stoddard RJ, Liu Y, Lin F, Shi X, Liu F, Hillhouse HW, Ginger DS, Chen H, Jen AKY. *Nat Nanotechnol*, 2022, 17: 53–60
12 Xian K, Cui Y, Xu Y, Zhang T, Hong L, Yao H, An C, Hou J. *J Phys Chem C*, 2020, 124: 7691–7698
13 Wang R, Zhang C, Li Q, Zhang Z, Wang X, Xiao M. *J Am Chem Soc*, 2020, 142: 12751–12759
14 Lee H, Park C, Sin DH, Park JH, Cho K. *Adv Mater*, 2018, 30: 1800453
15 Li T, Zhan X. *Acta Chim Sin*, 2021, 79: 257–283
16 Cheng S, Wang L, Guo C, Li D, Cai J, Miao W, Du B, Wang P, Liu D, Wang T. *Polymer*, 2021, 236: 124322
17 Sun R, Wang T, Wu Y, Zhang M, Ma Y, Xiao Z, Lu G, Ding L, Zheng Q, Brabec CJ, Li Y, Min J. *Adv Funct Mater*, 2021, 31: 2106846
18 Liao Q, Li B, Sun H, Koh CW, Zhang X, Liu B, Woo HY, Guo X. *Mater Rep-Energy*, 2021, 1: 100063
19 Yao J, Qiu B, Zhang ZG, Xue L, Wang R, Zhang C, Chen S, Zhou Q, Sun C, Yang C, Xiao M, Meng L, Li Y. *Nat Commun*, 2020, 11: 2726
20 Liu J, Liu Y, Wang J, Li H, Zhou K, Gui R, Xian K, Qi Q, Yang X, Chen Y, Zhao W, Yin H, Zhao K, Zhou Z, Ye L. *Adv Energy Mater*, 2022, 12: 2201975
21 Cui Y, Xu Y, Yao H, Bi P, Hong L, Zhang J, Zu Y, Zhang T, Qin J, Ren J, Chen Z, He C, Hao X, Wei Z, Hou J. *Adv Mater*, 2021, 33: 2102420
22 Chong K, Xu X, Meng H, Xue J, Yu L, Ma W, Peng Q. *Adv Mater*, 2022, 34: 2109516
23 Sun R, Wu Y, Yang X, Gao Y, Chen Z, Li K, Qiao J, Wang T, Guo J, Liu C, Hao X, Zhu H, Min J. *Adv Mater*, 2022, 34: 2110147
24 He C, Pan Y, Ouyang Y, Shen Q, Gao Y, Yan K, Fang J, Chen Y, Ma CQ, Min J, Zhang C, Zuo L, Chen H. *Energy Environ Sci*, 2022, 15: 2537–2544
25 Li N, Perea JD, Kassar T, Richter M, Heumueller T, Matt GJ, Hou Y, Güldal NS, Chen H, Chen S, Langner S, Berlinghof M, Unruh T, Brabec CJ. *Nat Commun*, 2017, 8: 14541
26 Ye L, Gao M, Hou J. *Sci China Chem*, 2021, 64: 1875–1887
27 Shi M, Wang T, Wu Y, Sun R, Wang W, Guo J, Wu Q, Yang W, Min J. *Adv Energy Mater*, 2021, 11: 2002709
28 Su Y, Zhang L, Ding Z, Zhang Y, Wu Y, Duan Y, Zhang Q, Zhang J, Han Y, Xu Z, Zhang R, Zhao K, Liu SF. *Adv Energy Mater*, 2022, 12: 2103940
29 Jørgensen M, Norrman K, Gevorgyan SA, Tromholt T, Andreasen B, Krebs FC. *Adv Mater*, 2012, 24: 580–612
30 Peters IM, Hauch J, Brabec C, Sinha P. *Joule*, 2021, 5: 3137–3153
31 Cheng P, Zhan X. *Chem Soc Rev*, 2016, 45: 2544–2582
32 Burlingame Q, Ball M, Loo YL. *Nat Energy*, 2020, 5: 947–949
33 Xian K, Geng Y, Ye L. *Joule*, 2022, 6: 941–944
34 Malla RB, Brown KM. *Acta Astronaut*, 2015, 107: 196–207
35 Hsieh YJ, Huang YC, Liu WS, Su YA, Tsao CS, Rwei SP, Wang L. *ACS Appl Mater Interfaces*, 2017, 9: 14808–14816
36 Feng G, Li J, He Y, Zheng W, Wang J, Li C, Tang Z, Osvet A, Li N, Brabec CJ, Yi Y, Yan H, Li W. *Joule*, 2019, 3: 1765–1781
37 Chen F, Zhang Y, Wang Q, Gao M, Kirby N, Peng Z, Deng Y, Li M, Ye L. *Chin J Chem*, 2021, 39: 2570–2578
38 Müller C. *Chem Mater*, 2015, 27: 2740–2754
39 Yang W, Luo Z, Sun R, Guo J, Wang T, Wu Y, Wang W, Guo J, Wu Q, Shi M, Li H, Yang C, Min J. *Nat Commun*, 2020, 11: 1218
40 Lai H, Chen H, Zhou J, Qu J, Wang M, Xie W, Xie Z, He F. *J Phys Chem Lett*, 2019, 10: 4737–4743
41 Zhu L, Zhang M, Zhou G, Hao T, Xu J, Wang J, Qiu C, Prine N, Ali J, Feng W, Gu X, Ma Z, Tang Z, Zhu H, Ying L, Zhang Y, Liu F. *Adv Energy Mater*, 2020, 10: 1904234
42 Ma Y, Wang P, Lin W, Wang W, Cai D, Zheng Q. *Chem Eng J*, 2022, 432: 134393
43 Xian K, Liu Y, Liu J, Yu J, Xing Y, Peng Z, Zhou K, Gao M, Zhao W, Lu G, Zhang J, Hou J, Geng Y, Ye L. *J Mater Chem A*, 2022, 10: 3418–3429
44 Zhang Y, Ji Y, Zhang Y, Zhang W, Bai H, Du M, Wu H, Guo Q, Zhou E. *Adv Funct Mater*, 2022, 32: 2205115
45 Li D, Sun C, Yan T, Yuan J, Zou Y. *ACS Cent Sci*, 2021, 7: 1787–1797
46 Li C, Fu H, Xia T, Sun Y. *Adv Energy Mater*, 2019, 9: 1900999

47 Wang J, Zhang M, Lin J, Zheng Z, Zhu L, Bi P, Liang H, Guo X, Wu J, Wang Y, Yu L, Li J, Lv J, Liu X, Liu F, Hou J, Li Y. *Energy Environ Sci*, 2022, 15: 1585–1593
48 Chen J, Cao J, Liu L, Xie L, Zhou H, Zhang J, Zhang K, Xiao M, Huang F. *Adv Funct Mater*, 2022, 32: 2200629
49 Hong L, Yao H, Wu Z, Cui Y, Zhang T, Xu Y, Yu R, Liao Q, Gao B, Xian K, Woo HY, Ge Z, Hou J. *Adv Mater*, 2019, 31: 1903441
50 Grimme S, Antony J, Ehrlich S, Krieg H. *J Chem Phys*, 2010, 132: 154104
51 Takacs CJ, Sun Y, Welch GC, Perez LA, Liu X, Wen W, Bazan GC, Heeger AJ. *J Am Chem Soc*, 2012, 134: 16597–16606
52 Yang D, Jiao Y, Yang L, Chen Y, Mizoi S, Huang Y, Pu X, Lu Z, Sasabe H, Kido J. *J Mater Chem A*, 2015, 3: 17704–17712
53 Li M, Zhou Y, Zhang J, Song J, Bo Z. *J Mater Chem A*, 2019, 7: 8889–8896
54 Ye L, Hu H, Ghasemi M, Wang T, Collins BA, Kim JH, Jiang K, Carpenter JH, Li H, Li Z, McAfee T, Zhao J, Chen X, Lai JLY, Ma T, Bredas JL, Yan H, Ade H. *Nat Mater*, 2018, 17: 253–260
55 Ye L, Li S, Liu X, Zhang S, Ghasemi M, Xiong Y, Hou J, Ade H. *Joule*, 2019, 3: 443–458
56 Yang C, Zhang S, Ren J, Gao M, Bi P, Ye L, Hou J. *Energy Environ Sci*, 2020, 13: 2864–2869
57 Gao J, Ma X, Xu C, Wang X, Son JH, Jeong SY, Zhang Y, Zhang C, Wang K, Niu L, Zhang J, Woo HY, Zhang J, Zhang F. *Chem Eng J*, 2022, 428: 129276
58 Koster LJA, Kemerink M, Wienk MM, Maturová K, Janssen RAJ. *Adv Mater*, 2011, 23: 1670–1674
59 Gupta V, Kyaw AKK, Wang DH, Chand S, Bazan GC, Heeger AJ. *Sci Rep*, 2013, 3: 1965
60 Kyaw AKK, Wang DH, Gupta V, Leong WL, Ke L, Bazan GC, Heeger AJ. *ACS Nano*, 2013, 7: 4569–4577
61 Cui Y, Yao H, Hong L, Zhang T, Tang Y, Lin B, Xian K, Gao B, An C, Bi P, Ma W, Hou J. *Natl Sci Rev*, 2020, 7: 1239–1246
62 Ma X, Wang J, Gao J, Hu Z, Xu C, Zhang X, Zhang F. *Adv Energy Mater*, 2020, 10: 2001404
63 Mukherjee S, Herzing AA, Zhao D, Wu Q, Yu L, Ade H, DeLongchamp DM, Richter LJ. *J Mater Res*, 2017, 32: 1921–1934
64 Ye L, Xiong Y, Li S, Ghasemi M, Balar N, Turner J, Gadisa A, Hou J, O'Connor BT, Ade H. *Adv Funct Mater*, 2017, 27: 1702016
65 Mukherjee S, Jiao X, Ade H. *Adv Energy Mater*, 2016, 6: 1600699
66 Baker JL, Jimison LH, Mannsfeld S, Volkman S, Yin S, Subramanian V, Salleo A, Alivisatos AP, Toney MF. *Langmuir*, 2010, 26: 9146–9151
67 Page KA, Kusoglu A, Stafford CM, Kim S, Kline RJ, Weber AZ. *Nano Lett*, 2014, 14: 2299–2304
68 Johnston DE, Yager KG, Hlaing H, Lu X, Ocko BM, Black CT. *ACS Nano*, 2014, 8: 243–249
69 Hlaing H, Lu X, Hofmann T, Yager KG, Black CT, Ocko BM. *ACS Nano*, 2011, 5: 7532–7538
70 Ma L, Yao H, Wang J, Xu Y, Gao M, Zu Y, Cui Y, Zhang S, Ye L, Hou J. *Angew Chem Int Ed*, 2021, 60: 15988–15994
71 Xiao Y, Lu X. *Mater Today Nano*, 2019, 5: 100030
72 Ma Y, Zhang M, Wan S, Yin P, Wang P, Cai D, Liu F, Zheng Q. *Joule*, 2021, 5: 197–209
73 Chaney TP, Levin AJ, Schneider SA, Toney MF. *Mater Horiz*, 2022, 9: 43–60
74 Peng Z, Ye L, Ade H. *Mater Horiz*, 2022, 9: 577–606
75 Shen X, Hu W, Russell TP. *Macromolecules*, 2016, 49: 4501–4509
76 Qin Y, Balar N, Peng Z, Gadisa A, Angunawela I, Bagui A, Kashani S, Hou J, Ade H. *Joule*, 2021, 5: 2129–2147
77 Liang Z, Li M, Wang Q, Qin Y, Stuard SJ, Peng Z, Deng Y, Ade H, Ye L, Geng Y. *Joule*, 2020, 4: 1278–1295
78 Yuan X, Zhao Y, Xie D, Pan L, Liu X, Duan C, Huang F, Cao Y. *Joule*, 2022, 6: 647–661
79 Gasparini N, Paleti SHK, Bertrandie J, Cai G, Zhang G, Wadsworth A, Lu X, Yip HL, McCulloch I, Baran D. *ACS Energy Lett*, 2020, 5: 1371–1379
80 Hultmark S, Paleti SHK, Harillo A, Marina S, Nugroho FAA, Liu Y, Ericsson LKE, Li R, Martín J, Bergqvist J, Langhammer C, Zhang F, Yu L, Campoy-Quiles M, Moons E, Baran D, Müller C. *Adv Funct Mater*, 2020, 30: 2005462
81 Lee JW, Sun C, Kim DJ, Ha MY, Han D, Park JS, Wang C, Lee WB, Kwon SK, Kim TS, Kim YH, Kim BJ. *ACS Nano*, 2021, 15: 19970–19980
82 Li F, Yager KG, Dawson NM, Jiang YB, Malloy KJ, Qin Y. *Chem Mater*, 2014, 26: 3747–3756